

Quantitative exploration of the bright and dark exciton landscape and fine structure of MoS₂ (using G₀W₀-BSE)

Hongyu Yu,^{1,2} Magdalena Laurien,^{1,*} Zhenpeng Hu,² and Oleg Rubel^{1,†}

¹*Department of Materials Science and Engineering, McMaster University,
1280 Main Street West, Hamilton, Ontario L8S 4L7, Canada*

²*School of Physics, Nankai University, Tianjin 300071, China*

(Dated: June 4, 2022)

Abstract

Spectral ordering between of dark and bright excitons in transition metal dichalcogenides is of increasing interest for optoelectronic applications. However, little is known about dark exciton energies and their binding energies. We report the exciton landscape including momentum-forbidden dark excitons of MoS₂ monolayer using single shot GW-Bethe Salpeter equation (G₀W₀-BSE) calculations. We find the lowest-energy exciton to be indirect at ($K'_v \rightarrow K_c$) in agreement with recent GdW-BSE calculations [2D Mater. 6, 035003 (2019)]. We also find that by large, dark exciton binding energies (E_b) scale with the quasiparticle energies (E_g) according to the $E_b/E_g = 0.25$ rule. Differences in exciton binding energies are explained using an orbital theory.

I. INTRODUCTION

Two-dimensional transition metal dichalcogenides (TMDCs) like monolayer (ML) MoS_2 exhibit an intricate electronic fine structure that offers an abundance of possibilities to manipulate their optical and electrical properties and exploit them for novel devices. A fascinating aspect of ML materials that sets them apart from their bulk equivalents is the behavior of excitations: Quasi-particles formed of an excited electron and a hole (excitons) experience a greater Coulomb attraction in a monolayer material because of the lack of screening in the third dimension. These excitonic effects dominate the optical response of ML TMDCs.

Excitons can be either bright (optically accessible) or dark (optically inaccessible). Dark excitons can be classified according to two main characteristics: spin and location in momentum space of the electron and hole. Spin-forbidden dark excitons are quasiparticles where the electron and the hole occupy the same position in momentum space, however, their spin is opposite and thus radiative recombination is not possible. Momentum-forbidden dark excitons consist of an electron and a hole located at different points in momentum space. Unassisted recombination is not possible for these indirect excitons either, thus they are dark.

Besides the bright states, dark excitons have a considerable influence on the optical response of TMDC MLs.¹ For example, spectral closeness of dark excitons to bright excitons can cause a significant drop of the photoluminescent yield in ML MoS_2 .² Similarly, higher-energy momentum-forbidden dark excitons can serve as a reservoir of charge carriers for bright transitions that are lower in energy and thus enhance the response for TMDC MLs³. Indirect excitons have also been related to the achievable degree of circular polarization in TMDC MLs⁴ and the formation of quantum dots in bilayer WSe_2 .⁵ In addition, dark excitons in WSe_2 can be activated or brightened, i.e. the photoluminescence intensity increases, in the presence of a magnetic field which leads to the creation of bright excitons with long and tunable life times.^{6,7} Brightening can also be achieved by strain⁸ or the adsorption of high-dipole molecules⁹, allowing for completely new device concepts in the design of high-sensitivity sensors.

Knowledge of the spectral relation of dark and bright excitons is important to fully understand the optical response of monolayer TMDCs.^{1,10} This is especially crucial for ML MoS_2 for which the ordering of the lowest-energy bright and dark excitons is still being discussed^{11–13}. The spectral ordering of bright and dark excitons depends mainly on the amount of band splitting caused by spin-orbit coupling as well as difference of the exciton binding energies. Initially, the empha-

sis was placed on studying direct excitons.¹⁴ However, comprehensive quantitative studies of the excitonic landscape including indirect, finite-momentum excitons are scarce. Important contributions were made first by Malic *et al.*¹⁵ who calculated the optical response of group-VI TMDCs. They emphasized the importance of excitonic corrections to the band structure that can lead to a change of the band character from direct to indirect or affect the ordering of bright and dark states. However, their results showed only qualitative trends. Berghäuser *et al.*¹⁶ obtained the exciton landscape of monolayer MoS₂ and other group-VI TMDCs using pump-probe experiments and an empirically parameterized quantum model. According to their study, the lowest-energy state for ML MoS₂ is a dark (indirect) exciton with its hole located at Γ_v and the electron located at K'_c ($\Gamma_v \rightarrow K'_c$). Very recently, Deilmann and Thygesen¹⁷ reported calculations of the exciton landscape including indirect excitons in the GdW+BSE scheme, where the approximation $dW = W - W_{\text{metal}}$ enables a higher computational efficiency¹⁸. They found the excitonic state of monolayer MoX₂ to be dark (indirect) and located at $K_v \rightarrow K'_c$.

In this report, we use *ab initio* calculations [single-shot GW (G_0W_0) + BSE beyond the Tamm-Dancoff approximation (TDA)] to explore the whole bright and dark excitonic landscape of ML MoS₂ to contribute to the ongoing discussion. According to our results, the exciton ground state is a dark indirect exciton at $K_v \rightarrow K'_c$. We show that even spin-forbidden and indirect excitons obey the universal relationship between exciton energy and exciton binding energy proposed for bright excitons in ML 2D materials¹⁹ and discuss the variations in the binding energies in the light of orbital theory.

II. METHODS

A. G_0W_0 +BSE calculations

We performed G_0W_0 -BSE *ab initio* calculations. The procedure for GW-BSE calculations is as follows: In the GW step the electronic ground state previously obtained using density functional theory²⁰ is corrected for quasiparticle effects. This correction is obtained by solving for the self-energy which includes the many-body exchange-correlation interactions in a single shot. In Hedin's method²¹, the self-energy is approximated by the product of the one-particle Green's function G and the screened Coulomb potential W . The quasiparticle corrected energies and wave functions are used as input for the BSE which describes interactions of particle-hole pairs and

directly yields the optical excitation energies. The exciton wave function is constructed as an expansion in terms of quasiparticle wave functions, and then the BSE can be solved self-consistently as an eigenvalue problem. In most cases, it is sufficient to solve the BSE in the TDA^{22–24}.

$$(E_{c\mathbf{k}+\mathbf{Q}} - E_{v\mathbf{k}}) A_{v\mathbf{k}}^{(S,\mathbf{Q})} + \sum_{v'c'k'} K_{v\mathbf{k},v'c'k'}^{AA}(\mathbf{Q}) A_{v'c'k'}^{(S,\mathbf{Q})} = \Omega^{(S,\mathbf{Q})} A_{v\mathbf{k}}^{(S,\mathbf{Q})}. \quad (1)$$

Here $\Omega^{(S,\mathbf{Q})}$ is the exciton energy (the eigenvalue), $E_{v\mathbf{k}}$ ($E_{c\mathbf{k}+\mathbf{Q}}$) are the energies of the valence band (conduction band) obtained in the GW step, $A_{v\mathbf{k}}^{(S,\mathbf{Q})}$ are expansion coefficients for the exciton wave function, and K is the interaction kernel which contains all the electron-hole interactions. Details concerning the mathematical form of K can be found in Leng *et al.*²⁴. The index \mathbf{Q} denotes a momentum transfer by a certain \mathbf{Q} vector. Here, we went beyond the TDA, including resonant-antiresonant coupling (K^{AB} , K^{BA}):²⁴

$$\left\{ \begin{array}{l} (E_{c\mathbf{k}+\mathbf{Q}} - E_{v\mathbf{k}}) A_{v\mathbf{k}}^{(S,\mathbf{Q})} + \sum_{v'c'k'} K_{v\mathbf{k},v'c'k'}^{AA}(\mathbf{Q}) A_{v'c'k'}^{(S,\mathbf{Q})} \\ \quad + \sum_{v'c'k'} K_{v\mathbf{k},v'c'k'}^{AB}(\mathbf{Q}) B_{v'c'k'}^{(S,\mathbf{Q})} = \Omega^{(S,\mathbf{Q})} A_{v\mathbf{k}}^{(S,\mathbf{Q})} \\ (E_{c\mathbf{k}+\mathbf{Q}} - E_{v\mathbf{k}}) B_{v\mathbf{k}}^{(S,\mathbf{Q})} + \sum_{v'c'k'} K_{v\mathbf{k},v'c'k'}^{BB}(\mathbf{Q}) B_{v'c'k'}^{(S,\mathbf{Q})} \\ \quad + \sum_{v'c'k'} K_{v\mathbf{k},v'c'k'}^{BA}(\mathbf{Q}) A_{v'c'k'}^{(S,\mathbf{Q})} = \Omega^{(S,\mathbf{Q})} B_{v\mathbf{k}}^{(S,\mathbf{Q})} \end{array} \right. \quad (2)$$

Where $B_{v\mathbf{k}}^{(S,\mathbf{Q})}$ are expansion coefficients for the antiresonant part of the exciton wave function.

The main reason to conduct calculations beyond the TDA for our work was that the software used does not allow the calculation of finite-momentum excitons within the TDA. Further, the TDA has been shown to break down for nanoscale systems^{25–27}. The TDA has also been shown to deviate from experiment for finite-momentum excitons in silicon.²⁸ Though we do not expect the resonant-antiresonant coupling to have a great effect on the optical properties of a ML TMDC, going beyond the TDA might lead to more accurate results.

To the best of our knowledge, solving the BSE beyond the TDA has not yet been reported for group-VI metal transition dichalcogenides. In the following we describe the details of our settings used to perform the G_0W_0 -BSE beyond TDA calculations.

B. Computational details

Our calculations were performed with the Vienna ab initio package (VASP)^{29,30}, version 5.4.4. The projector-augmented wave method^{31,32} was used to treat core and valence electrons with 14

electrons for Mo, and 6 electrons for S explicitly included in the valence states. The plane-wave energy cutoff was set to 400 eV. Recommended GW projector-augmented wave potentials supplied by VASP were employed for all atoms. The Perdew-Burke-Ernzerhof³³ exchange-correlation functional was used to obtain the electronic ground state with density functional theory^{34,35}. To ensure minimal interlayer coupling, monolayers were separated by 21.5 Å of vacuum which is sufficient for the longitudinal component of the macroscopic static dielectric tensor to be close to unity. Atomic positions and lattice vectors were fully relaxed with a tolerance of 0.01 eV/Å. Only the c vector (out-of-plane vector) was fixed during the relaxation procedure. Electronic minimization was performed with a tolerance of 10^{-7} eV and convergence accelerated with Gaussian smearing of the Fermi surface by 0.05 eV. The Brillouin zone was sampled with a $12 \times 12 \times 1$ Γ -centered k -point mesh in order to include high symmetry points in the k mesh and ensure sufficient accuracy of the exciton binding energy that is highly dependent on the density of the k mesh³⁶. After structure relaxation, we obtained a lattice constant of 3.185 Å, a metal-chalcogen (M-X) bond length of 2.414 Å, and a chalcogen-chalcogen X-X bond length of 3.12838 Å. The obtained lattice constant is close to the experimental lattice constant of bulk MoS₂ ($a = 3.16$ Å)^{37–39} and in excellent agreement with other computational studies^{40–42}. The M-X bond length is in very good agreement with experimental data^{43,44}.

For all calculations following the relaxation procedure, we considered spin-orbit coupling and included 640 bands (26 of them occupied) in order to have enough empty bands for the ensuing GW calculations. We calculated the quasiparticle band structure at the single-shot G_0W_0 level of theory. For the response function we set a cutoff of 250 eV (VASP-tag ENCUTGW); this parameter controls how many G-vectors are included in the GW-calculation. The number of frequency grid points was set to 96 (VASP-tag NOMEGA). For visualizing the quasiparticle band structure we applied Wannier interpolation using the WANNIER90 program⁴⁵. The BSE calculations were carried out beyond the Tamm-Dancoff approximation using the full BSE Hamiltonian²⁸, which means that resonant-antiresonant coupling is included (VASP-tag ANTIREES=2). For solving the BSE, we considered 6 occupied bands and 8 virtual (unoccupied) bands of the quasiparticle band structure as a basis for excitonic eigenstates. To obtain finite-momentum excitons, we iterated over all possible \mathbf{Q} vectors that could be selected for the given k mesh in the first Brillouin zone (in total 144) and additional \mathbf{Q} vectors outside the first Brillouin zone to include the $\mathbf{K}'_v \rightarrow \mathbf{K}_c$, $\mathbf{K}_v \rightarrow \mathbf{K}'_c$ and $\mathbf{K}'_v \rightarrow \Lambda_c$ transitions. For all \mathbf{Q} vectors, we obtained the lowest 100 eigenstates as output (VASP-tag NBSEEIG).

Further, the orbitals were enforced to have real values at the Gamma point and points at the edge of the Brillouin zone (VASP-tag LORBITALREAL=true). The symmetry was turned off (VASP-tag ISYM=-1) as demanded by the LORBITALREAL-tag.

For post processing we used Python 3 with the Numpy, Pandas, Matplotlib packages. From the BSE output file (VASP: BSEFATBAND file) that contains the wave function of the exciton in momentum space for each BSE eigenstate with its BSE eigenvalues (exciton energies), we obtained the k-point with the biggest contribution to the exciton wave function (highest amplitude) for each eigenstate. This k-point was treated as the momentum vector of the hole of the exciton. The direct and indirect quasiparticle band gaps (without excitonic effect) were obtained from the band energies of the GW calculation. Exciton binding energies were then calculated by subtracting the BSE eigenvalues from the GW band gap matching the position of hole and electron of the exciton in momentum space. Oscillator strengths were extracted from the the general VASP output file (vasprun.xml).

To distinguish between spin-parallel and spin-antiparallel states, the spinor up and down components (α and β) were determined from spin projections (VASP: PROCAR file) as described in Refs. 46,47.

III. RESULTS AND DISCUSSION

The quasiparticle band structure of monolayer MoS₂ is shown in Fig. 1. The bands are obtained by Wannier interpolation of the GW eigenvalues. The band structure shows a direct band gap at the K and K' points. These points are equivalent (except for their spin) because of the time-reversal symmetry. Besides K and K', Λ and Λ' are related via time-reversal symmetry. For future discussions we will only refer to one of the via time-reversal symmetry related transitions.

The conventional way of plotting the band structure is neither convenient nor clear for presenting the electronic structure including excitonic effects. The band structure plot cannot capture a renormalization of the eigenvalues caused by direct, indirect, and dark excitons at the same time. To represent bright as well as spin- and momentum-forbidden dark excitons and their respective binding energies in one graph, we plot the exciton band structure in a two-dimensional fashion. In Fig. 2 the landscape of bright and dark excitons in ML MoS₂ is shown for the most important points in momentum space. To accommodate momentum forbidden dark excitons, the k vectors of the electron and hole of an exciton are displayed separately on the two axes of the

graph. Further, we distinguish between spin-up and spin-down states to allow for the visualization of spin-forbidden excitons. As a result, bright excitons are seen on the dashed red diagonal line, spin-forbidden direct excitons are on the dotted blue line, and momentum-forbidden excitons are located to the sides. Also, spin-allowed excitons are distributed at the lower left and upper right quarter while spin-forbidden excitons being placed at the upper left and lower right quarter. Each bubble represents an exciton; the colour displays the exciton energy and the radius of the bubble corresponds to the exciton binding energy. The time-reversal symmetry of the exciton is reflected as center symmetry in the graph. The symmetry of the wave function Φ of the exciton can be expressed as:

$$\Phi(\mathbf{k}_h, \mathbf{k}_e, \mathbf{s}_h, \mathbf{s}_e) = \Phi^*(-\mathbf{k}_h, -\mathbf{k}_e, -\mathbf{s}_h, -\mathbf{s}_e). \quad (3)$$

As a result, excitons $|\mathbf{k}_h, \mathbf{k}_e, \mathbf{s}_h, \mathbf{s}_e\rangle$ and $|\mathbf{k}_h, \mathbf{k}_e, \mathbf{s}_h, \mathbf{s}_e\rangle$ should have the same properties. As necessitated by our procedure, we calculated the whole BZ irrespective of time reversal symmetry. Computational inaccuracies of the order of 1 meV for the band energies [and for the K (K') point exciton energies] between per definition of time reversal symmetry identical states. We reinstated time reversal symmetry in the graph by selecting the exciton with the lower energy.

The exciton with the largest binding energy of 0.712 eV (marked with a spade) is located at $\Gamma_v \downarrow$ (hole) and $\Lambda'_c \downarrow$ (electron) ($\Gamma_v \downarrow \rightarrow \Lambda'_c \downarrow$). The lowest-energy exciton (marked with a star) has an energy of 1.793 eV and is located at $K_v \downarrow \rightarrow K'_c \downarrow$. This implies that after considering excitonic effects, we find a change of the optical band gap location of MoS₂ with regards to the transport band gap: the optical band gap is now indirect. The exciton at $K_v \downarrow \rightarrow K'_c \downarrow$ is 6 meV lower in energy than the bright exciton at K and 1 meV lower in energy than the spin-forbidden direct exciton at K. The energy difference between the indirect exciton at K – K' and the direct spin-forbidden exciton at K – K (about 1 meV) is within the range of computational uncertainty. Thus, at our level of theory we cannot predict with certainty whether the indirect or direct and spin-forbidden transition at the K valleys constitutes the lowest exciton. The band ordering is illustrated in Fig. 3.

Besides the evaluation of the spin-states, dark and bright excitons can be distinguished by their oscillator strength. The oscillator strength of bright excitons is several magnitudes higher than of dark excitons¹². In Fig. 4 we show the oscillator strength (bubble size) obtained from solving the BSE paired with the quasiparticle band gap (colour map) in a similar fashion to the exciton landscape. We find that the direct, spin-allowed excitons at K and K' are about 1400 times higher in oscillator strength than their spin-forbidden equivalents.

Strikingly, large oscillator strengths appear for the indirect and spin-forbidden transitions at $K - K'$ (e.g. $K_v \downarrow \rightarrow K'_c \uparrow$) (Fig. 4). The oscillator strengths are in the order of magnitude of the direct bright $K_v \downarrow \rightarrow K_c \downarrow$ transitions. We are uncertain how to interpret these results: An attempt of a physical explanation is to look at the Coulomb electron-hole exchange^{48–50}. In this exchange interaction, electrons and holes of excitons in the K and K' valley mix, creating quasi-bright indirect K - K' transitions. This mixing does not require additional momentum transfer or spin-flips¹⁴. However, a failure of the software might as well be responsible for the large oscillator strengths.

Figure 4 also shows that our GW calculations predict a direct band gap at K , the valence and conduction band having the same spin. The lower-energy spin-forbidden excited state after considering excitonic effects arises due to different exciton binding energies (E_b) of the dark and the bright exciton: The E_b of the dark exciton ($E_b = 0.637$ eV) is about 13 meV higher than the binding energy of the bright exciton ($E_b = 0.624$ eV) while the spin splitting of the CB is only about 9 meV (see Fig. 3). Thus, after considering excitonic effects, the spin-forbidden transition at K is lower in energy than the spin-allowed transition. These results are in agreement with Qiu *et al.*¹¹ and Deilmann and Thygesen¹⁷ who also found the dark exciton at K to be lower in energy than the bright exciton. Echeverry *et al.*¹², using the GW-BSE method came to the opposite conclusion. Qiu *et al.*⁵¹ explain the differing results in the literature with different settings of the density functional theory, GW and BSE parameters.

We stress that because of the complexity of the calculations at the high level of theory, we cannot avoid dealing with underconverged properties. The G_0W_0 -BSE procedure as implemented in VASP and as used for this work does not provide the option to truncate the Coulomb interaction between periodic images. Carefully conducted studies^{51,52} show that Coulomb truncation is essential for achieving convergence of the GW band energy corrections, as without the truncation the periodic images of the monolayer increase the dielectric function, especially in the low- Q limit. Further, a very high k mesh up to $300 \times 300 \times 1$ is required in order to converge the exciton binding energy to within 0.1 eV⁵¹. As our G_0W_0 calculations and the BSE beyond TDA calculations were conducted without considering geometrical and time reversal symmetries, the computational cost precludes the use of high k meshes (due to excessive memory requirements). However, the errors of not truncating the Coulomb interaction and using a coarse k mesh partly cancel out.⁵²

The values obtained from our calculations for the band gap and exciton binding energies are in good agreement with experiment. Using scanning tunneling spectroscopy and optical reflectance

contrast measurements for MoS₂ on fused silica, Rigosi *et al.*⁵³ obtained a binding energy of the bright excitons of 0.31 ± 0.04 eV and an electronic band gap of 2.17 ± 0.1 eV. The results of our calculation with $E_b = 0.624$ eV and $E_g = 2.42$ eV are slightly higher than the experimental values because the calculations are obtained for a free-standing monolayer and a relatively coarse k mesh. Other computational studies using GW-BSE found results that are quite close to ours obtaining 2.42 eV for the band gap and 0.57 eV for bright exciton binding energy¹⁹. The difference in the E_b can be explained with the k mesh density: Jiang *et al.*¹⁹ used a k mesh of $16 \times 16 \times 1$ (our calculations: $12 \times 12 \times 1$) and the binding energy strongly depends on the k mesh³⁶.

Now we will discuss the binding energies of the whole exciton landscape in more detail. Fig. 5 shows the relationship between the quasiparticle band gap and exciton binding energy, including bright, spin-forbidden and momentum-forbidden excitons. Generally, excitons at large quasiparticle band gaps have larger exciton binding energies. We included a dashed line in the figure that represents the $E_b/E_g = 0.25$ rule for excitons of 2D materials proposed by Jiang *et al.*¹⁹. Momentum-allowed excitons follow the rule that the exciton binding energy is about 0.25 of quasiparticle band gap¹⁹ irrespective of their spin. Momentum-forbidden excitons also generally follow the trend of the exciton binding energy being about 0.25 of the band gap but with more scattering (ratios from 0.23 to 0.27).

We further note that most of the holes of the excitons locate at Γ or K and the electrons of the excitons locate at the Λ or K (see Fig. 2). Interestingly, the exciton binding energy of the excitons whose hole is at Γ is almost always higher than of excitons whose hole is located at K. For bulk semiconductors this effect could be explained with the effective mass differences as the effective mass of the hole at the Γ point is higher than that of the hole at the K point⁵⁴. However, for the binding energies of 2D materials the effective mass does not play a significant role, provided the polarizability is large (which is the case for MoS₂).^{19,54}

Further, it is well known that the high binding energy of 2D materials originates from the lack of screening in the third dimension. Hence, we expect one factor for the different binding energies to be differences in screening depending on the position of the electron in real space. To qualitatively compare the amount of screening experienced by different excitons, we performed an orbital analysis for the valence and conduction band states of each exciton. The basic idea is that electrons contained in orbitals pointing perpendicular to the layer experience less screening than electrons of orbitals confined within the plane of the monolayer. By convention, z is taken as the out-of-plane axis. It is well known, that for monolayer MoS₂ Γ_v exhibits high contributions of the

d_{z^2} and p_z orbitals while the K_v state is mainly composed of d_{xy} orbitals.⁴³ For our calculations we find the Γ_v state to consist of ca. 77 % d_{z^2} + 22 % p_z and the K_v state of 41 % d_{xy} + 41 % $d_{x^2-y^2}$. Thus we can expect excitons at Γ_v to experience less screening and consequently have higher binding energies than excitons at K_v .

IV. CONCLUSION

In conclusion, we performed calculations of finite-momentum excitons in MoS_2 monolayer within and beyond the first Brillouin zone. It is found that the holes of the lowest-energy excitons are located at the Γ or K valleys, while the electrons reside in the K or Λ valleys. Our calculations predict the lowest-energy exciton to be indirect at K - K' which is in agreement with recent GdW-BSE calculations¹⁷. However, the energy difference between the indirect exciton at K - K' and the spin-forbidden direct exciton at K - K is small (about 1 meV) and within the range of computational uncertainty. The bright exciton is located at K and 6 meV higher in energy than the lowest-energy exciton at K - K' . We also discussed the exciton binding energies. The ratio of $E_b/E_g = 0.25$ found for bright excitons in monolayer 2D materials holds true also for dark and indirect excitons. Stronger binding energies seem to be related to excitons contained in orbitals that point out of plane and thus experience less local screening.

ACKNOWLEDGMENTS

H.Y. acknowledges support by the National Science Fund of China for Talent Training in the Basic Sciences (No. J1103208). M.L. and O.R. acknowledge funding provided by the Natural Sciences and Engineering Research Council of Canada under the Discovery Grant Programs RGPIN-2015-04518. Calculations were performed using a Compute Canada infrastructure supported by the Canada Foundation for Innovation under John R. Evans Leaders Fund.

AUTHOR CONTRIBUTIONS

H.Y. and M.L. contributed equally to this work.

* laurienm@mcmaster.ca

† rubelo@mcmaster.ca

- ¹ T. Mueller and E. Malic, *npj 2D Materials and Applications* **2**, 29 (2018).
- ² F. Wu, F. Qu, and A. H. MacDonald, *Phys. Rev. B* **91**, 075310 (2015).
- ³ A. Steinhoff, M. Florian, M. Rösner, G. Schönhoff, T. Wehling, and F. Jahnke, *Nat. Commun.* **8**, 1166 (2017).
- ⁴ M. Baranowski, A. Surrente, D. K. Maude, M. Ballottin, A. A. Mitoglu, P. C. M. Christianen, Y. C. Kung, D. Dumcenco, A. Kis, and P. Plochocka, *2D Mater.* **4**, 025016 (2017).
- ⁵ J. Lindlau, M. Selig, A. Neumann, L. Colombier, J. Förste, V. Funk, M. Förg, J. Kim, G. Berghäuser, T. Taniguchi, *et al.*, *Nat. Commun.* **9**, 2586 (2018).
- ⁶ X.-X. Zhang, T. Cao, Z. Lu, Y.-C. Lin, F. Zhang, Y. Wang, Z. Li, J. C. Hone, J. A. Robinson, D. Smirnov, *et al.*, *Nat. Nanotechnol.* **12**, 883 (2017).
- ⁷ R. Vasconcelos, H. Bragança, F. Qu, and J. Fu, *Phys. Rev. B* **98**, 195302 (2018).
- ⁸ M. Feierabend, Z. Khatibi, G. Berghäuser, and E. Malic, *arXiv preprint arXiv:1806.07350* (2018).
- ⁹ M. Feierabend, G. Berghäuser, A. Knorr, and E. Malic, *Nat. Commun.* **8**, 14776 (2017).
- ¹⁰ M. Selig, G. Berghäuser, M. Richter, R. Bratschitsch, A. Knorr, and E. Malic, *2D Mater.* **5**, 035017 (2018).
- ¹¹ D. Y. Qiu, F. H. da Jornada, and S. G. Louie, *Phys. Rev. Lett.* **111**, 216805 (2013).
- ¹² J. P. Echeverry, B. Urbaszek, T. Amand, X. Marie, and I. C. Gerber, *Phys. Rev. B* **93**, 121107(R) (2016).
- ¹³ M. Molas, C. Faugeras, A. Slobodeniuk, K. Nogajewski, M. Bartos, D. Basko, and M. Potemski, *2D Mater.* **4**, 021003 (2017).
- ¹⁴ G. Wang, A. Chernikov, M. M. Glazov, T. F. Heinz, X. Marie, T. Amand, and B. Urbaszek, *Rev. Mod. Phys.* **90**, 021001 (2018).
- ¹⁵ E. Malic, M. Selig, M. Feierabend, S. Brem, D. Christiansen, F. Wendler, A. Knorr, and G. Berghäuser, *Phys. Rev. Materials* **2**, 014002 (2018).

- ¹⁶ G. Berghäuser, P. Steinleitner, P. Merkl, R. Huber, A. Knorr, and E. Malic, Phys. Rev. B **98**, 020301(R) (2018).
- ¹⁷ T. Deilmann and K. S. Thygesen, 2D Mater. **6**, 035003 (2019).
- ¹⁸ M. Drüppel, T. Deilmann, J. Noky, P. Marauhn, P. Krüger, and M. Rohlfing, Phys. Rev. B **98**, 155433 (2018).
- ¹⁹ Z. Jiang, Z. Liu, Y. Li, and W. Duan, Phys. Rev. Lett. **118**, 266401 (2017).
- ²⁰ W. Kohn and L. J. Sham, Phys. Rev. **140**, A1133 (1965).
- ²¹ L. Hedin, Phys. Rev. **139**, A796 (1965).
- ²² I. Tamm, in *Selected Papers* (Springer Berlin Heidelberg, 1991) pp. 157–174.
- ²³ S. M. Dancoff, Phys. Rev. **78**, 382 (1950).
- ²⁴ X. Leng, F. Jin, M. Wei, and Y. Ma, WIREs Comput. Mol. Sci. **6**, 532 (2016).
- ²⁵ Y. Ma, M. Rohlfing, and C. Molteni, Phys. Rev. B **80**, 241405(R) (2009).
- ²⁶ P. Puschnig, C. Meisenbichler, and C. Draxl, arXiv preprint arXiv:1306.3790 (2013).
- ²⁷ M. Gruning, A. Marini, and X. Gonze, Nano Lett. **9**, 2820 (2009).
- ²⁸ T. Sander, E. Maggio, and G. Kresse, Phys. Rev. B **92**, 045209 (2015).
- ²⁹ G. Kresse and J. Hafner, Phys. Rev. B **47**, 558 (1993).
- ³⁰ G. Kresse and J. Furthmüller, Comp. Mater. Sci. **6**, 15 (1996).
- ³¹ P. E. Blöchl, Phys. Rev. B **50**, 17953 (1994).
- ³² G. Kresse and D. Joubert, Phys. Rev. B **59**, 1758 (1999).
- ³³ J. P. Perdew, K. Burke, and M. Ernzerhof, Phys. Rev. Lett. **77**, 3865 (1996).
- ³⁴ P. Hohenberg and W. Kohn, Phys. Rev. **136**, B864 (1964).
- ³⁵ W. Kohn and L. J. Sham, Phys. Rev. **140**, A1133 (1965).
- ³⁶ M. Bokdam, T. Sander, A. Stroppa, S. Picozzi, D. D. Sarma, C. Franchini, and G. Kresse, Sci. Rep. **6**, 28618 (2016).
- ³⁷ K. Bronsema, J. De Boer, and F. Jellinek, Z. Anorg. Allg. Chem. **540**, 15 (1986).
- ³⁸ B. Schönfeld, J. Huang, and S. Moss, Acta Crystallogr., Sect. B: Struct. Sci **39**, 404 (1983).
- ³⁹ J. Wildervanck and F. Jellinek, Z. Anorg. Allg. Chem. **328**, 309 (1964).
- ⁴⁰ J. Kang, S. Tongay, J. Zhou, J. Li, and J. Wu, Appl. Phys. Lett. **102**, 012111 (2013).
- ⁴¹ G.-B. Liu, W.-Y. Shan, Y. Yao, W. Yao, and D. Xiao, Phys. Rev. B **88**, 085433 (2013).
- ⁴² A. Ramasubramaniam, Phys. Rev. B **86**, 115409 (2012).

- ⁴³ M. Samadi, N. Sarikhani, M. Zirak, H. Zhang, H.-L. Zhang, and A. Z. Moshfegh, *Nanoscale Horiz.* **3**, 90 (2018).
- ⁴⁴ R. G. Dickinson and L. Pauling, *J. Am. Chem. Soc.* **45**, 1466 (1923).
- ⁴⁵ A. A. Mostofi, J. R. Yates, Y.-S. Lee, I. Souza, D. Vanderbilt, and N. Marzari, *Comput. Phys. Commun.* **178**, 685 (2008).
- ⁴⁶ F. Giustino, *Materials modelling using density functional theory: properties and predictions* (Oxford University Press, 2014).
- ⁴⁷ C. Zheng, S. Yu, and O. Rubel, *Phys. Rev. Materials* **2**, 114604 (2018).
- ⁴⁸ T. Jakubczyk, V. Delmonte, M. Koperski, K. Nogajewski, C. Faugeras, W. Langbein, M. Potemski, and J. Kasprzak, *Nano Lett.* **16**, 5333 (2016).
- ⁴⁹ M. Glazov, E. Ivchenko, G. Wang, T. Amand, X. Marie, B. Urbaszek, and B. Liu, *Phys. Status Solidi B* **252**, 2349 (2015).
- ⁵⁰ T. Yu and M. W. Wu, *Phys. Rev. B* **89**, 205303 (2014).
- ⁵¹ D. Y. Qiu, F. H. da Jornada, and S. G. Louie, *Phys. Rev. B* **93**, 235435 (2016).
- ⁵² F. Hüsler, T. Olsen, and K. S. Thygesen, *Phys. Rev. B* **88**, 245309 (2013).
- ⁵³ A. F. Rigosi, H. M. Hill, K. T. Rim, G. W. Flynn, and T. F. Heinz, *Phys. Rev. B* **94**, 075440 (2016).
- ⁵⁴ T. Olsen, S. Latini, F. Rasmussen, and K. S. Thygesen, *Phys. Rev. Lett.* **116**, 056401 (2016).

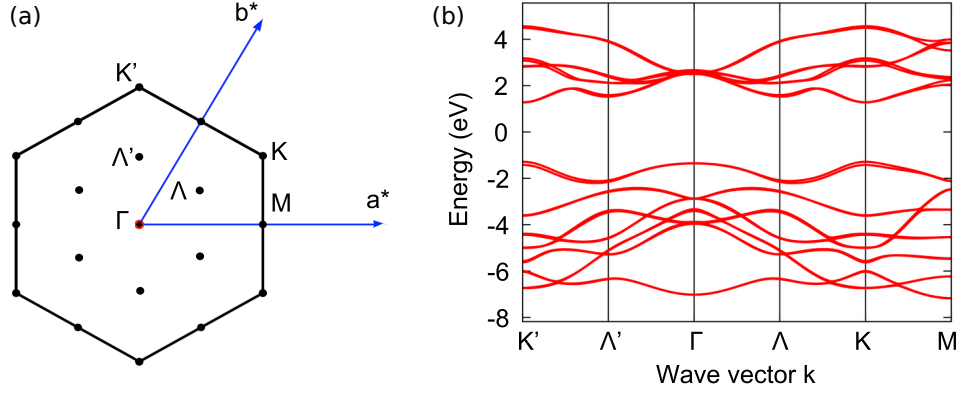


FIG. 1. (a) First Brillouin zone of monolayer MoS₂ and (b) quasiparticle band structure after Wannier-interpolation. The direct band gap is located at K (K').

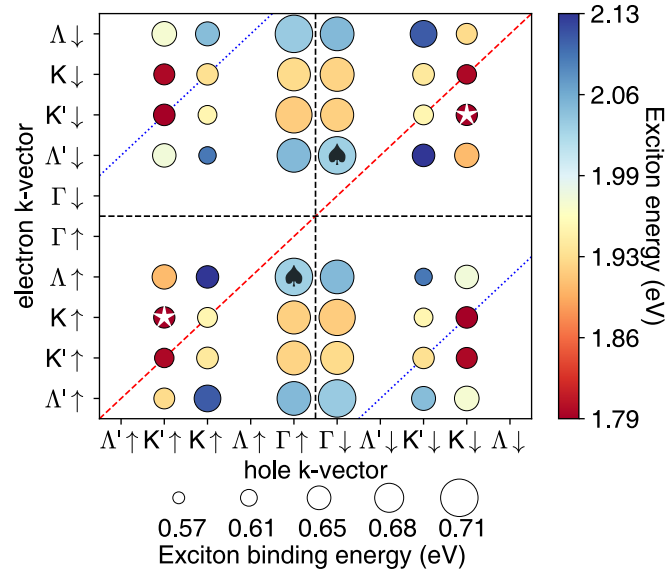


FIG. 2. MoS₂ exciton landscape including dark and bright excitons. The color scale reflects the exciton energy and the circle size represents the exciton binding energy. In order to display finite-momentum excitons, hole and electron k vectors are displayed separately on the horizontal and vertical axis, respectively. The lowest-energy exciton (star) is located at $K'_v \uparrow \rightarrow K_c \uparrow$ and is therefore momentum-forbidden. The highest binding energy (spades) occurs for an indirect exciton at $\Gamma_v \downarrow \rightarrow \Lambda'_c \downarrow$.

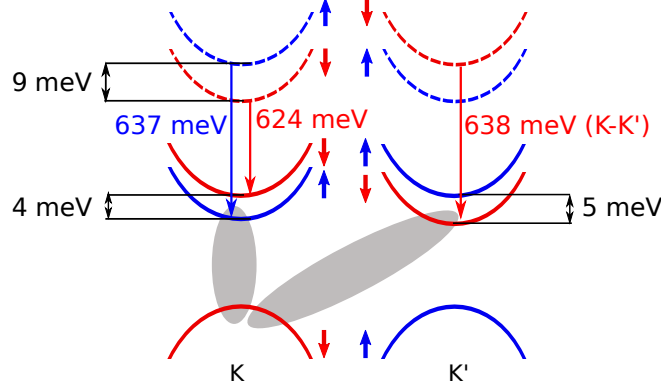


FIG. 3. Schematic diagram of the lowest-energy excitons at the K-K' valley of ML MoS₂. The ordering of solid energy bands corresponds to the exciton-corrected energies. The dashed conduction bands denote the quasiparticle band ordering. The lowest-energy exciton is either indirect and located at K-K' or spin-forbidden and direct at K (with the energy difference of 1 meV). This result is linked to differences in the exciton binding energies which are higher for the spin- and momentum-forbidden excitons than for the bright exciton (637, 638, and 624 meV, respectively).

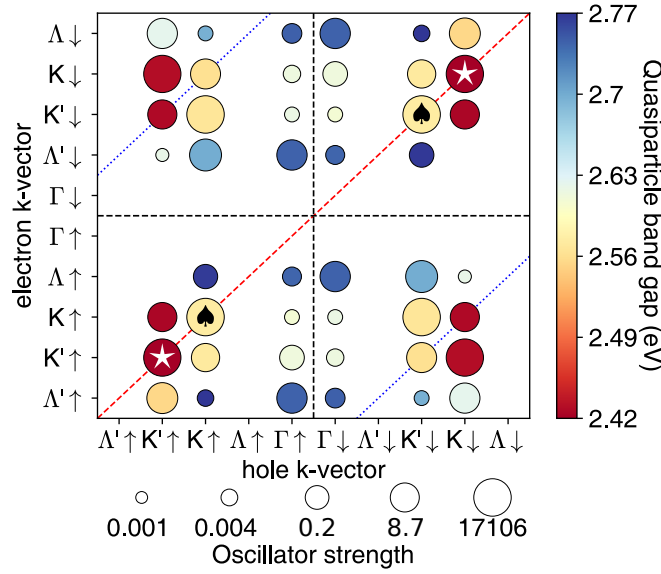


FIG. 4. MoS₂ quasiparticle band gaps (color scale) and oscillator strengths (bubbles in a log scale) for bright and dark excitons. The quasiparticle band gap is located at K ↓. The oscillator strength of the bright transitions is several magnitudes larger than that of dark transitions; the highest oscillator strength corresponds to the $K'_v \downarrow \rightarrow K'_c \downarrow$ transition. The oscillator strength of $K'_v \uparrow \rightarrow \Lambda_c \uparrow$ transition is about 10^{-4} which is too small to show.

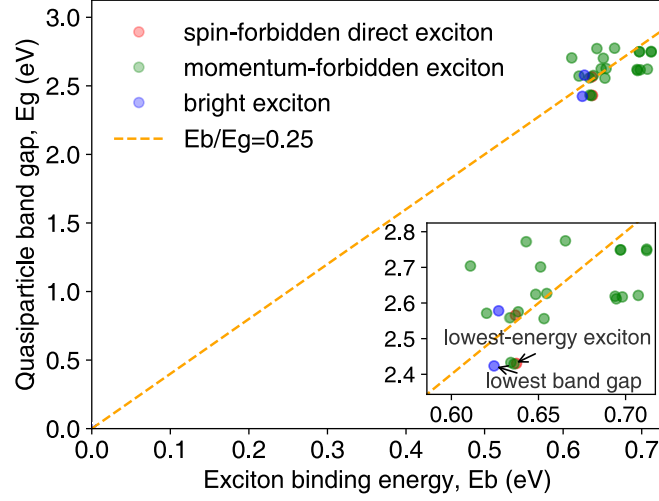


FIG. 5. Ratio of the exciton binding energy (E_b) and quasiparticle band gap (E_g) for MoS₂. Bright excitons (blue), spin-forbidden excitons (red) and momentum-forbidden excitons (green) are shown. The relationship of $E_b/E_g = 0.25$ according to Jiang *et al.*¹⁹ is shown by a dashed line. As a general trend, all excitons, including finite-momentum excitons, follow that rule.